

Dynamical signatures of Rossby vortices in cavity-hosting disks

C.M.T. Robert¹, H. Méheut¹, and F. Ménard²

¹ Université Côte d'Azur, Observatoire de la Côte d'Azur, CNRS, Laboratoire Lagrange, Bd de l'Observatoire, CS 34229, 06304 Nice cedex 4, FRANCE

² Univ. Grenoble Alpes, CNRS, IPAG, F-38000 Grenoble, FRANCE
e-mail: clement.robert@oca.eu

compiled July 17, 2020; Received –; accepted –

ABSTRACT

Context. Planets are formed amidst young circumstellar disks of gas and dust. The latter is traced by thermal radiation, where strong asymmetric clumps were observed in a handful of cases. These dust traps could be key to understand the early stages of planet formation, when solids grow from micron-size to planetesimals.

Aims. Vortices are among the few known asymmetric dust trapping scenarios. The present work aims at predicting their characteristics in a complementary observable. Namely, line-of-sight velocities are well suited to trace the presence of a vortex. Moreover, the dynamics of disks is subject to recent developments.

Methods. 2D hydro-simulations were performed where a vortex forms at the edge of a gas depleted region. We derived idealized line-of-sight velocity maps, varying disk temperature and orientation relative to the observer. The signal of interest, as a small perturbation to the dominant axisymmetric component in velocity, may be isolated in observational data using a proxy for the dominant quasi-Keplerian velocity. We propose that the velocity curve on the observational major axis be such a proxy.

Results. Applying our method to the disk around HD 142527 as a study case, we predict line-of-sight velocities scarcely detectable by currently available facilities, depending on disk temperature. We show that corresponding spirals patterns can also be detected with similar spectral resolutions, which will help discriminating against alternative explanations.

Key words. protoplanetary discs; hydrodynamics - instabilities; methods: numerical

1. Introduction

Planets are formed in circumstellar disks made mainly of gas and some solid dust components. Many aspects of the processes implied in their formation remain challenging to explain. More specifically, the transition from small dust grains to large planetesimals face two major obstacles: the drift barrier corresponding to fast inward drifting due to gas headwind, and the collision barrier due to destructive collisions (Chiang & Youdin 2010). Pressure bumps provide a solution to the drift barrier, as they act as a barrier stopping the drifting solids and forming dust rings. Indeed, concentric dusty rings are a common feature in resolved infrared images of protoplanetary disks (Andrews et al. 2018). Pressure bumps are also known to promote the formation of large scale vortices, through the Rossby Wave Instability (RWI), that are proposed as a solution to the barriers in planetesimal formation. They both stop the dust drift and harness efficient growth by lowering relative speeds between grains. This is why vortices were proposed as a planet-promoting scenario (Barge & Sommeria 1995; Adams & Watkins 1995; Tanga et al. 1996; Bracco et al. 1999). Moreover, it is well known that massive planets build up pressure bumps in their vicinity, exciting vortex formation (de Val-Borro et al. 2006, 2007; Fu et al. 2014; Hammer et al. 2017; Andrews et al. 2018; Baruteau et al. 2019), which in turn affects planetary migration (Regály et al. 2013; Ataiee et al. 2014; McNally et al. 2018). The study of large vortices is thus key to understand planetary formation.

The RWI (Lovelace et al. 1999; Li et al. 2000, 2001) is a promising vortex-forming scenario, and is expected where sharp density gradients are found. So-called "transitional" disks pro-

vide such conditions at the outer edge of large (~ 5 AU to 100 AU) gas cavities they host. Extensive computational effort has been dedicated to studying long term evolution of RWI vortices (Fu et al. 2014; Méheut et al. 2012a; Regály & Vorobyov 2017b; Andrews et al. 2018). Overall, eddies tend to form in a few tenth of orbital periods and survive for 10^3 to 10^4 orbital periods.

Concurrently, asymmetric dust crescents are being observed in thermal radiation of a growing number of targets (Cazzolletti et al. 2018; Dong et al. 2018; Isella et al. 2018; Casassus et al. 2019; Pineda et al. 2019) as well as in scattered emission (Benisty et al. 2018). Those clumps are candidates for large vortices, and there have been attempts to explain their formation as vortex-driven (Regály et al. 2012; Birnstiel et al. 2013). Alternatively, disk eccentricity (Ataiee et al. 2013) and excitation by an eccentric companion (Price et al. 2018) were proposed to explain these azimuthal dust excess, however not reproducing the observed dust-to-gas ratio.

Complementary measurements of the gas dynamics would be of great help in constraining and rejecting concurrent explanations. Continuum emission traces the spatial distribution of dust grains dynamically coupled with the gas, so it provides indirect information on the underlying gas dynamics. However, direct measurements of the gas radial velocity can now be achieved through Doppler-shifting of molecular lines, thanks to increasingly sophisticated data reduction techniques (Yen et al. 2016; Teague et al. 2016; Teague & Foreman-Mackey 2018), and even enhanced spatial resolution (Andrews et al. 2018). It is becoming possible to use these data to build connections to continuum asymmetries (Casassus et al. 2015b; Casassus & Pérez 2019)

or searching for planet-induced deviations (Pinte et al. 2018; Teague et al. 2018a; Pinte et al. 2019; Pérez et al. 2020).

Hence, observations in molecular line emission are key to confirm or reject current and future vortex candidates. The present paper is aimed at characterizing the dynamical signatures expected for a single large Rossby eddy forming in the inner rim of a cavity, by the means of hydro simulations.

The paper is organized as follows. First, we describe the numerical setup of our hydro simulations in Section 2. We then provide insight on the observability of resulting vortices and propose a method to extract their signature from observational data in Section 3. Finally, we discuss the limits of our approach in Section 4 and conclude in Section 5.

2. Hydro simulations setup

Using MPI-AMRVAC 2.2 (Porth et al. 2014; Xia et al. 2018), we perform 2D hydro simulations. Namely, we solve Euler equations for an inviscid gas

$$\partial_t \Sigma + \nabla \cdot (\Sigma \mathbf{v}) = 0, \quad (1)$$

$$(\partial_t + \mathbf{v} \cdot \nabla) \Sigma \mathbf{v} = -\Sigma \nabla \phi - \nabla p, \quad (2)$$

where Σ and \mathbf{v} stand for surface density and velocity respectively, $\phi \propto -1/r$ is a central gravitational potential and p is the vertically integrated pressure. It is prescribed by a barotropic equation of state $p = S\Sigma^\gamma$ where $S = 86.4$ code units¹ characterizes the entropy and $\gamma = 5/3$ is the adiabatic index. Sound speed is given as $c_s^2 = \gamma p / \Sigma$. Equations are solved on a linearly spaced polar grid (r, φ) with a fixed resolution $(512, 512)$, ranging from $r_{\min} = 75$ AU to $r_{\max} = 450$ AU and $\varphi \in [0, 2\pi]$. (Numerical convergence was checked against runs with double resolution in each direction) MPI-AMRVAC 2.2 use finite-volumes Riemann solvers. A two-step hllc integration scheme (Harten et al. 1983) and a Koren slope limiter (Koren 1993) are used in our simulations.

The model is physically inviscid. The numerical viscosity, expressed in terms of the widely used " α "-paradigm (Shakura & Sunyaev 1973), was estimated to lie between $2 \times 10^{-8} \leq \alpha \leq 3 \times 10^{-4}$ in the vortex-forming region. Details on this estimations are given in Appendix B.

The disk is truly "massless" in that both self-gravity and indirect terms due to the barycenter's motion are neglected in the computation of the gravitational potential. Zhu & Baruteau (2016) showed that including either or both of these contributions affects the vortex's evolution. In particular, the inclusion of indirect terms promotes a radial displacement of the structure and overall increases the density contrast with respect to its background. This latter result was also confirmed by Regály & Vorobyov (2017a) for vortices formed in a viscosity transition region. Because of these combined effects, the velocity of the structure is also modified, while a direct comparison is non-trivial.

2.1. Initial conditions

The initial gas surface density features a smooth radial density jump, modeling a disk cavity as

$$\Sigma(r, t = 0) = \Sigma_0 (r/r_*)^{-1} \times \frac{1}{2} \left[1 + \tanh \frac{r - r_j}{\sigma_j} \right], \quad (3)$$

¹ Our code unit system is completely described by mass, length and time normalisation constants respectively $m_* = 1$ solar mass, $r_* = 100$ AU and $t_* = 1$ orbital period of a test particle at $r = r_j$.

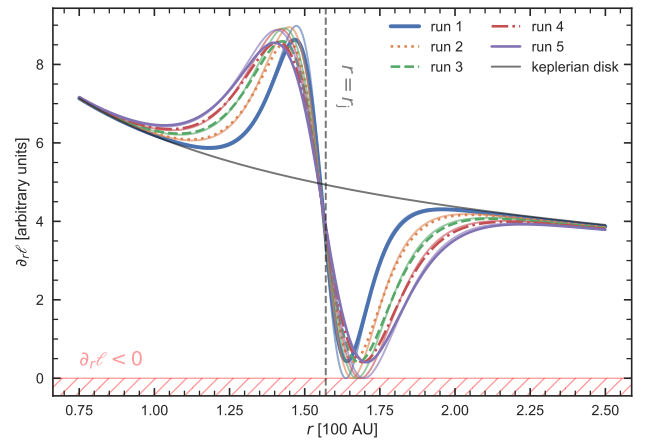


Fig. 1. Initial gradient in specific angular momentum ℓ for our 5 simulations (thick lines, ranked from coldest to hottest) compared to the keplerian case. The width of the density "jump" region σ_j is adjusted in two steps. First, we derive the critical value σ_j^{crit} for which the global minimum in $\partial_r \ell$ is exactly 0 (thin solid lines). Any value $\sigma_j < \sigma_j^{\text{crit}}$ would give rise to a rotationally unstable region, characterized by $\partial_r \ell < 0$. We then take an arbitrary 5% margin and set $\sigma_j = 1.05 \times \sigma_j^{\text{crit}}$ in our runs (thick dashed lines).

where r_j and σ_j are the radial location and the width of the jump respectively, and $r_* = 100$ AU is a normalisation factor. The initial equilibrium azimuthal velocity is defined as

$$\frac{v_\varphi^2}{r} = \frac{GM}{r^2} + \frac{\partial_r p}{\Sigma}, \quad (4)$$

where G is the universal gravity constant and M is the mass of the central star.

Observational constraints for HD 142527 are used to tune numerical values, wherever applicable, as we will now detail. We assume $M = 2.2 M_\odot$, compatible with existing estimations (Verhoeff et al. 2011; Casassus et al. 2015a). We choose a standard radial density slope in r^{-1} , which is also compatible with estimate from Verhoeff et al. (2011) in the optically thin approximation at 1 mm. Distance to star is now known with good precision 157 ± 7 pc thanks to Gaia Collaboration et al. (2016), which implies the cavity lies at $r_j = 157$ AU for an angular size of $1''.0$ (Casassus et al. 2012). The reference setup has an aspect-ratio, or "temperature"² $h \equiv H(r_j)/r_j \simeq 0.09$, where $H(r)$ is the disk scale height.

Other simulations with $h \in [0.09; 0.16]$ were performed, and labeled run 1 to run 5 by increasing value in h . They are discussed in Section 3.3. The derivation of this parameter is detailed in Appendix A.1. As this temperature is varied, we adjust the density jump's width σ_j within 5% of its critical value, where the disk becomes rotationally unstable under Rayleigh's criterion (Rayleigh 1879). Doing so, we approach the physical upper limit in vortex velocity after the RWI saturates. The corresponding signature in the specific angular momentum $\ell = rv_\varphi$ is illustrated in Fig. 1. The computed values for σ_j , and for runs from 1 to 5, are [11.6, 14.7, 16.9, 18.7, 20.2] AU. Even in the hottest case, the simulation box extends at least $4\sigma_j$ away from the density jump center r_j . Unless explicitly stated, all figures show the results for the reference model.

² The disk's vertical spreading is physically caused by heating, and usually characterized by a scale height.

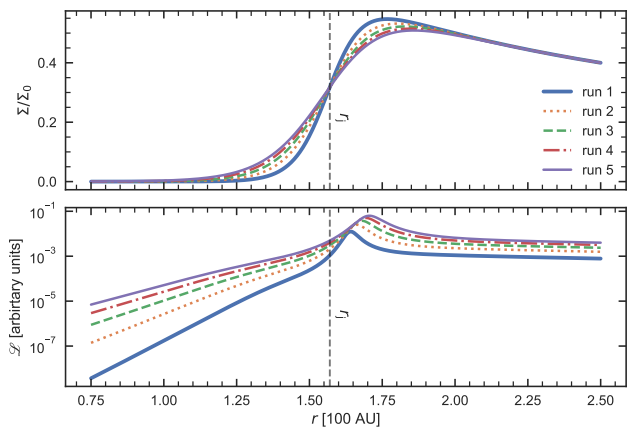


Fig. 2. Initial radial profiles in surface density (top) and the $\mathcal{L}(r)$ function (defined in Eq. (5)) for our 5 simulations. In each model, $\mathcal{L}(r)$ features a clear local maximum, which is a necessary condition to RWI growth.

2.2. Boundary conditions

Boundary conditions are imposed through ghost cells outside of the domain and wave killing region in the active domain. In the radial direction, ghost cells are fixed to the initial equilibrium values for density and azimuthal momentum. The radial momentum is copied from the first cells to the ghost cells at inner boundary, and extrapolated linearly with no-inflow condition at outer edge. However, these boundary conditions have low impact as standard damping zones (de Val-Borro et al. 2006) are also used to avoid reflections at domain edges. The domain is periodic in the azimuthal direction.

2.3. The Rossby wave instability & vortex formation

RWI is similar to the Kelvin-Helmholtz instability in a differentially rotating Keplerian disk. It tends to convert excess shear into vorticity. Lovelace et al. (1999) showed that a local extremum in the background potential vorticity is a necessary condition to the RWI. More recent works clarified that a minimum is required (Lai & Tsang 2009; Ono et al. 2016). The key function is defined as

$$\mathcal{L}(r) = \frac{1}{2} \frac{\Sigma}{(\nabla \times \mathbf{v}) \cdot \mathbf{e}_z} S^{2/\gamma}. \quad (5)$$

We exhibit this key function within our initial setup in Fig. 2, showing the existence of a local maximum in $\mathcal{L}(r)$, corresponding to a minimum in vorticity.

We find that, in order to excite the RWI unstable modes, it is useful to add random perturbations. We chose to perturb the radial velocity, which is zero otherwise, as

$$v_r(r, \varphi, t = 0) = c_s \psi(r, \varphi) \exp \frac{-(r - r_j)^2}{2\sigma_j^2}, \quad (6)$$

where $\psi(r, \varphi) \in [-10^{-2}, 10^{-2}]$ is a uniformly distributed random variable drawn for each grid cell. After the instability has saturated, we obtain a single vortex shown in Fig. 3. In a frame co-rotating with the vortex, its global structure is quasi-stationary as shown in Fig. 4. The radial density profile at the azimuth of the density maximum is plotted at different times. The orange dotted curve at $t = 10$ features the most noticeable fluctuations,

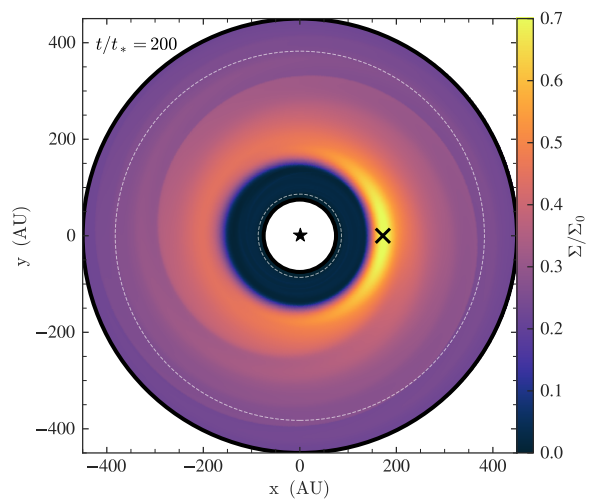


Fig. 3. Gas surface density plotted in Cartesian coordinates (x, y) after $t = 200$ orbital periods (t_*). The global density maximum is indicated by a black cross. The position of the central star is marked as a "★" symbol. The simulation box radial limits are drawn as solid black circles, while dashed-line circles indicate the limits of wave damping zones.

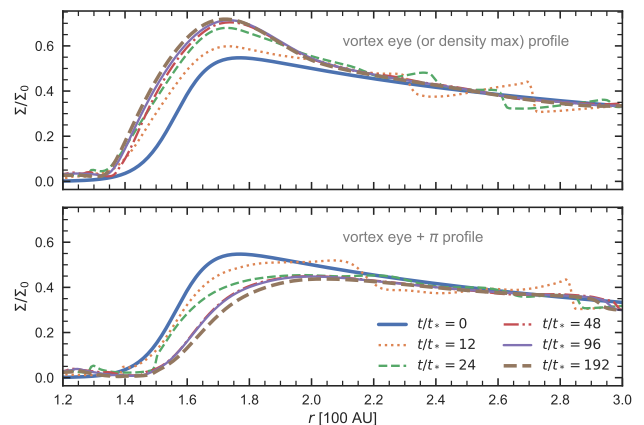


Fig. 4. Time evolution of the radial density profile, plotted as slices at the azimuth of the density maximum where the vortex eye lies (top) and its radial opposite (bottom). The slices correspond to the $y = 0$ axis in Fig. 3, with $x > 0$ (top) and $x < 0$ (bottom) respectively. After ~ 40 orbital periods, the disk has practically reached a stationary state. The cavity profile itself has become uneven, showing a non-zero eccentricity.

as smaller eddies are still undergoing a merger, and strong spiral waves are launched outwards. After 40 orbital periods, the surface density of the vortex is stabilized and does not rapidly evolve any more. Thus we will consider this state as quasi-stationary, as we take a look at the dynamics of the structure in the next section.

3. Vortex signatures in dynamics

In this section, we provide observational signatures obtained from the vortex's dynamics. The observable studied here is the velocity projected along the line of sight v_{LOS} . We first discuss an adequate decomposition of the velocity field to characterize the signatures. We then study their observability against disk orientation, and provide insight on how disk aspect ratio affects observed velocities.

3.1. Extracting dynamical signatures

The dynamics of a disk is dominated by rotation around the central star. In an axisymmetric stationary state, the net radial force is zero, as in Eq. (4). Due to pressure gradients, the radial equilibrium slightly departs from Keplerian motion. This is the sub-keplerian rotation in a disk with negative radial pressure gradient. As a dynamical structure, a vortex exposes little difference to global rotation. Thus, it is useful to decompose the angular velocity v_ϕ as

$$v_\phi = \langle v_\phi \rangle + (v_\phi - \langle v_\phi \rangle) \equiv \langle v_\phi \rangle + v'_\phi, \quad (7)$$

where $\langle \cdot \rangle$ is the azimuthal average operator, and we denote the non-axisymmetric part as v'_ϕ . Hence the total velocity field \mathbf{v} can be decomposed in the polar basis ($\mathbf{e}_r, \mathbf{e}_\phi$) as

$$\mathbf{v} = v_r \mathbf{e}_r + (\langle v_\phi \rangle + v'_\phi) \mathbf{e}_\phi \equiv \langle v_\phi \rangle \mathbf{e}_\phi + \mathbf{v}', \quad (8)$$

In the absence of a global accretion flow, there is no relevant axisymmetric part in v_r . Hence we consider that dynamical signatures of non-axisymmetric features reside in $\mathbf{v}' = v_r \mathbf{e}_r + v'_\phi \mathbf{e}_\phi$. Both components of this residual radial and azimuthal velocity are quantified in Fig. 5, and are of similar amplitudes. For comparison, the typical Keplerian speed at the vortex position ($r \sim 180$ AU) is $v_K = 3.3 \text{ km s}^{-1}$, one to two orders of magnitudes larger than the deviation due to the vortex, and one order of magnitude larger than the local sound-speed c_s . The amplitude in the azimuthal velocity is as high as 300 m s^{-1} for this reference (coldest) model. This sets a first upper limit to the spectral resolution required for a direct detection to about 100 m s^{-1} . This is achievable for bright lines with ALMA, e.g., for the CO (2-1) or the CO (3-2) transitions by using channel widths of 70 kHz or 120 kHz (or narrower), respectively. For example, van der Marel et al. (2016) successfully detected the ^{13}CO (3-2) and C^{18}O (3-2) lines of SR21, HD 135344B, DoAr44, and IRS 48 with good signal-to-noise (SNR) ratio (peak SNR in the integrated intensity map up to 30 for the ^{13}CO line) with spectral resolution of 0.1 km s^{-1} and angular resolution of $0''.25$. Boehler et al. (2017) obtained data with similar angular and spectral resolutions for HD 142527 but with much higher SNR. All sources are well detected in the lines and increasing the spectral resolution by another factor of 2, as well as the SNR, is possible within a reasonable amount of time (< 12 hours). We note that, there is a non-zero azimuthal velocity deviation at the maximum density/pressure (i.e. $v'_\phi \neq 0$), as seen in Fig. 5. Indeed, the vortex being an asymmetric structure, the radial position of the pressure extremum varies with the azimuth. Consequently, the line of exact keplerian rotation is not circular as shown in Fig. 5.

However, the decomposition proposed in Eq. (8) is vain unless the proposed dominant term $\langle v_\phi \rangle$ can be subtracted from observations. While a Keplerian fit is usually a suiting approximation of the dominant velocity term, it proves insufficient near sharp density jumps. As shown in Fig. 6 (a, b), subtracting a Keplerian power law leaves systematic velocities caused by pressure gradients. In the density transition region, those systematics dominate over the variability in the remaining signal.

However, we further show (Fig. 6 (b, c)) that averaging two facing cross sections in azimuthal velocities consistently yields a much better approximation for the global azimuthal average $\langle v_\phi \rangle$, with a standard deviation $\leq 20 \text{ m s}^{-1}$. This is a direct sign that the non-axisymmetric parts of the azimuthal velocities v'_ϕ in opposing disk halves are anticorrelated, although not strictly equal in amplitudes. Given that on the disk's observational major

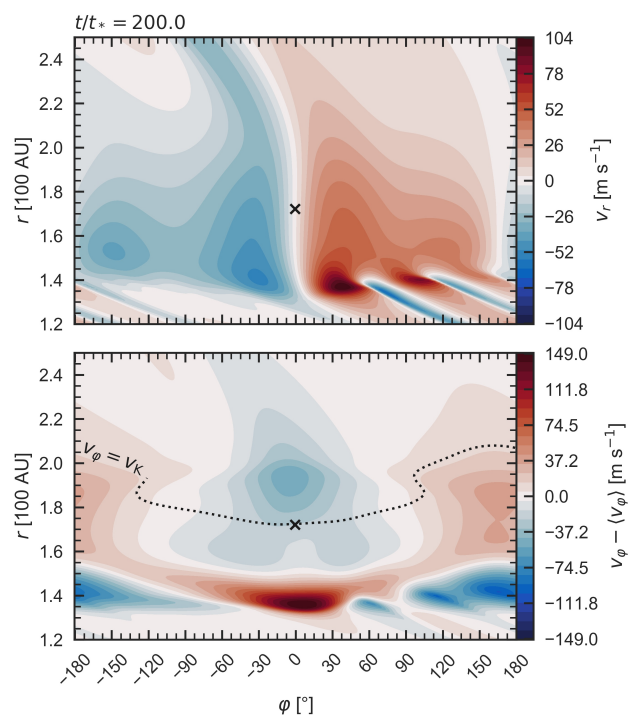


Fig. 5. Polar components of a vortex's velocity field. *Top*: radial velocity. *Bottom*: azimuthal velocity, where the axisymmetric part $\langle v_\phi \rangle$ is carried out. The pressure maximum is indicated by a black cross. The snapshot is taken at $t = 200$ orbital periods. A dotted line in the bottom panel indicates fluid in exact Keplerian rotation.

axis x , detection is only sensitive to azimuthal velocities, we naturally obtain a satisfying method to subtract $\langle v_\phi \rangle$ from the whole signal. Consequently, we will now confidently assume that the axisymmetric part $\langle v_\phi \rangle$ of the azimuthal velocity can indeed be removed with good precision from observations, and will only consider the remaining components of \mathbf{v}' exhibited in Fig. 5.

3.2. Vortex detection in line-of-sight velocities

Gas velocity is usually detected through Doppler-shifting in molecular lines. It is therefore the velocity component parallel to the line of sight that is probed. Within optically thick lines, the resulting velocity profile can be blurred by vertical integration over disk height. It is beyond the scope of the present work to inquire on this second-order effect, so we neglect both optical and geometrical thickness effects. This approach is reasonable within the assumption that emissive molecular regions are geometrically thin and well resolved (as remarked by Teague et al. (2018b)). Furthermore, full 3D simulations showed that, in a stationary state, a vortex tends to be tubular and that its vertical velocity is negligible (Lin 2012; Zhu & Stone 2014; Richard et al. 2013). This comforts us in the idea that, for long lived vortices, it is reasonable to ignore this component⁴. To study vortex dynamical signatures, we use here cylindrical coordinates centered on the star. The radial axis ($\phi = 0$) is the observational major-axis,

³ Inspiration for this figure was drawn from Teague et al. (2018a).

⁴ This also means we ignore the vertical extension in the conical shape of the emissive layer. However, it can easily be shown that for inclinations lower than 45° , even a very high emissive layer $z \approx 5H$ and a large aspect ratio $H/r = 0.2$, can in principle be deprojected as long as it remains spatially thin

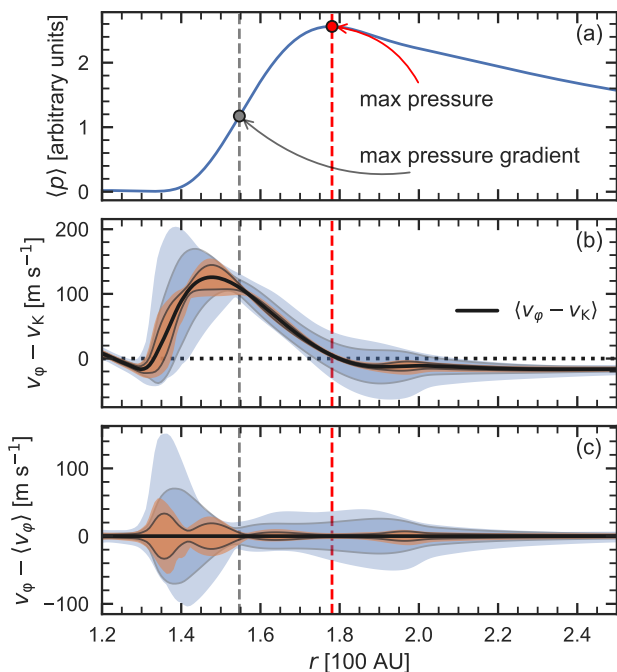


Fig. 6. A comparison between Keplerian velocity v_K and average azimuthal velocity $\langle v_\varphi \rangle$ as 1D masks. **(a):** pressure profile in arbitrary units. **(b and c):** azimuthal velocity cross-sections, with offsets (masks) v_K and $\langle v_\varphi \rangle$ respectively. The average $\langle V - \text{mask} \rangle$ is indicated by a thick black line, while shadows show the amplitude and standard deviations in blue ($V = v_\varphi$), and orange ($V = \frac{1}{2}(v_{\varphi,\text{left}} + v_{\varphi,\text{right}})$). Data is taken at $t = 200$ orbital periods.³

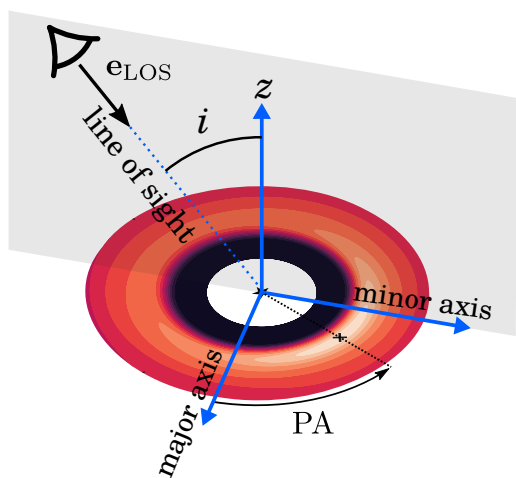


Fig. 7. A sketch view of our notations. A grey shadow shows the plane containing the vertical e_z and the line of sight.

and the upper part of the disk ($z > 0$) is defined to be the one seen by the observer Fig. 7.

Thus, the line-of-sight direction $\mathbf{e}_{\text{LOS}}(i, \varphi)$, defined as pointing away from the observer, can be written in the disk cylindrical basis ($\mathbf{e}_r, \mathbf{e}_\varphi, \mathbf{e}_z$) as

$$\mathbf{e}_{\text{LOS}}(i, \varphi) = -(\sin(i) \cos(\varphi) \mathbf{e}_r + \sin(i) \sin(\varphi) \mathbf{e}_\varphi + \cos(i) \mathbf{e}_z), \quad (9)$$

and it follows that the line-of-sight velocity corresponding to \mathbf{v}' writes

$$v'_{\text{LOS}} \equiv \mathbf{v}' \cdot \mathbf{e}_{\text{LOS}} = -\sin(i) (\sin(\varphi) v_r + \cos(\varphi) v'_\varphi). \quad (10)$$

Hence, the effective observable v'_{LOS} mixes v_r and v_φ . For a 2D vortex disk inclination equally affects all projected velocities and only acts as a scaling factor $\sin(i)$. An inclination $i = 27^\circ$, corresponding to the estimated value for HD 142527 (Fukagawa et al. 2013), is used in the following applications. This choice is arbitrary and used as a textbook case. We note that this inclination is moderate. Deprojection would still be feasible at up to $i = 45^\circ$, where projected velocities would be 1.5 times larger, making detection easier. Figure 8 shows the morphology of the observable v'_{LOS} (large panels), along with corresponding components v_r and v'_φ (small panels), for four different values of PA. This result constitutes an idealized case, built on the assumption that the axisymmetric component $\langle v_\varphi \rangle$ can be exactly subtracted from observational data. At all position angles (PAs), the vortex's anticyclonic motion around the density maximum is apparent in v'_{LOS} ⁵. This point roughly coincides with the maximum luminosity at most wavelengths, and can be located within continuum observations, if not directly in molecular lines used to infer projected velocities.

We note that the vortex's eye and the region immediately facing it have similar Doppler shifts (e.g. both blue at PA = 0°). This is an expected outcome of subtracting the azimuthally averaged velocity, since the both regions are local extrema along the azimuthal direction. Another signature of the vortex is the azimuthal proximity between the maximum density (black cross) and the projected velocity extrema (color dots). The later two points are determined by the physical on-site velocity as well as the system's inclination, and hence are virtual positions. Their physical separation is maximized for PA = 90° and minimized for PA = 0°. A direct implication is that detecting a vortex lying on the major axis requires greater angular resolution. However, little dependency of the velocity range on the PA is found. The topography of the signal changes with the PA but the anticyclonic region stands out regardless the orientation. The signature is also typical with a sign reversal in the vicinity of the pressure maximum, along the major-axis direction. This characteristic behaviour, sign change, is easier to measure in relative than the absolute small velocities and would be observed even with a beam covering the vortex almost entirely (about 100 AU, or 0''.6 in the case of HD 142527).

3.3. Detectability against disk temperature

Although our setup is constrained by observations, its temperature (or equivalently h) is not. Indeed the temperature gives the sound-speed, which is key in estimating the vortex velocity. In order to study this dependency, four additional simulations with higher temperatures ($h \in [0.094, 0.119, 0.136, 0.150, 0.161]$) were performed. In Fig. 9, we show contours of projected velocity v'_{LOS} , sampled at an interval corresponding to a tenth of the obtained dynamical range, namely 10 m s⁻¹. The reference, "coldest" setup produces the lowest velocities ranging from -20 to +20 m s⁻¹, where most of the "detected" structure is within the vortex region. The direct observation of a peak-to-valley velocity shift of about 40 m s⁻¹ is challenging but is within reach of ALMA. Bohler et al. (2017) observed HD 142527 for a total of 4 hours during Cycle 1, targeting the continuum and ¹³CO (3-2) and C¹⁸O (3-2) lines with a spectral resolution of 110 m s⁻¹ (after Hanning smoothing). The disk is detected in both lines at high SNR. The angular resolution of the observations was 45 AU (beam 0''.27 × 0''.31). The presence of a velocity signature is cur-

⁵ We are set in the particular case where the PA "rotates" in the same direction as the disk. When not so, sign in v'_{LOS} must simply be inverted.

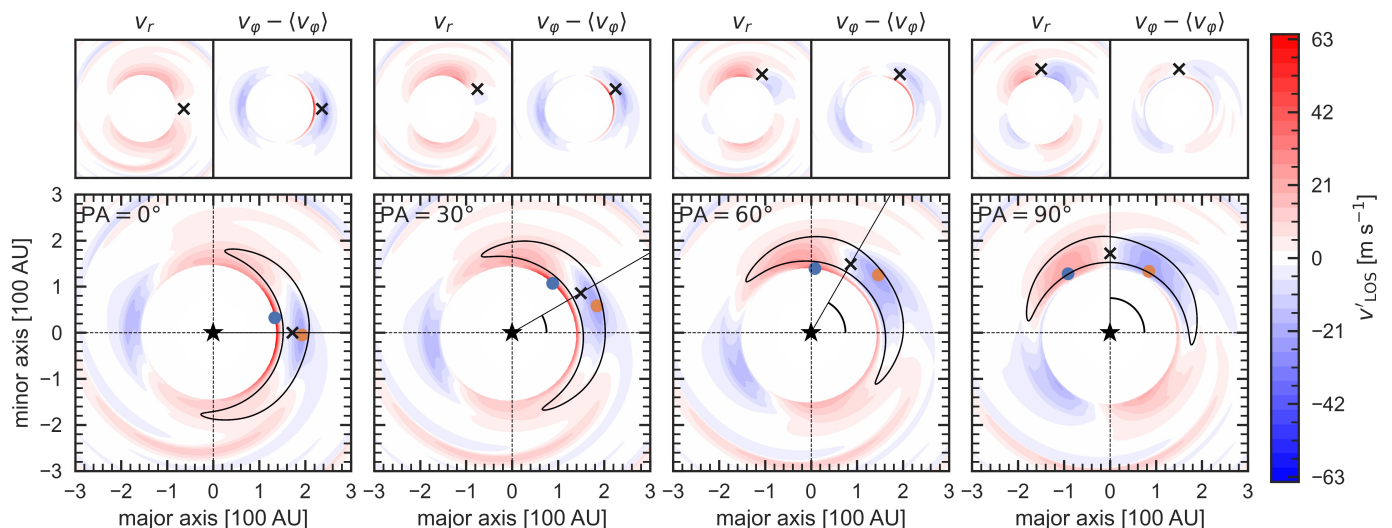


Fig. 8. Line-of-sight velocities (bottom large panels) as defined in Eq. (10), applied to HD 142527 with $i = 27^\circ$, and varying PA. Top panels exhibit the corresponding polar components. Color reflects implied Doppler-shifts in molecular lines. Blue/orange dots indicate extreme values in v'_{LOS} . In the leftmost panel, the vortex’s spatial extension is shown as a solid contour which corresponds to $\Sigma = 0.5\Sigma_0$, where Σ_0 is the scaling factor used in Eq. (3). The inner cavity, where fast spiral waves are launched but surface density is low, is not shown here: regions with $\Sigma/\Sigma_0 < 0.1$ are masked. As a proxy for the vortex’s eye, a black cross indicates the density maximum.

rently being investigated in that data set (Boehler et al, in prep.). This angular resolution is sufficient to resolve the vortex in HD 142527 and the spectral resolution can be improved by a factor of 2 on the brighter ^{12}CO line (Perez et al. 2015), or on the ^{13}CO and C^{18}O lines by increasing the time spent on-source.

At higher temperatures, more structure is revealed as the spiral arm unravels. Figure 10 shows the v'_{LOS} variation amplitude, against temperature (left panel) and time (right panel). Although the upper bound of this range consistently increases with temperature, we note that the mean value is almost unchanged from run 4 to run 5. Indeed, in runs 3 to 5, the amplitude of time-variations are significantly higher than for the reference run. These large variations are related with the life-cycle of a secondary spiral arm that appears in hot cases, as illustrated in Fig. 11. However, because this secondary spiral is most prominent when the disk itself becomes visibly eccentric it is likely that this structure would be affected, be the indirect gravitational terms taken included in the model. A conservative conclusion is that only the lower boundary of the variation interval should be taken into account. Additionally, we observe that between runs 4 and 5, the dynamical range stagnates at 94 m s^{-16} . This saturation is likely caused by the instability in the cavity’s eccentricity, thus we infer that validity of massless disk models is disputable in the hottest case (run 5). We note that a previous study of the gas dynamics in HD 142527 (Casassus et al. 2015a) did not provide evidence of any strong asymmetric structure, this may indeed be due to a lack of spectral resolution ($\sim 1 \text{ km s}^{-1}$).

3.4. RWI spirals

Spirals structures are detected in HD 142527 (Fukagawa et al. 2006; Casassus et al. 2012; Rameau et al. 2012; Avenhaus et al. 2014; Christiaens et al. 2014). Several scenario have been proposed to understand their origin, such as self-gravitational instability (SGI), excitation by the stellar companion (Billler et al. 2012; Price et al. 2018), connection to a shadow cast by a mis-

⁶ Indeed, this is the range shown in Fig. 9, where the simulations are shown at a time that minimizes it ($t/t_* = 200$).

aligned inner disk (Montesinos et al. 2016), or a combination of several effects (Christiaens et al. 2014). Spirals are also a natural outcome of the RWI, as Rossby waves are coupled to spiral density waves in a Keplerian disk. Such spiral waves would have the same frequency as the Rossby wave creating the vortex.

As opposed to companion-excited spirals, those are not caused by gravitational interaction and are observed in massless disks simulations such as ours (Huang et al. 2019). For Rossby vortices, the launching point is radially close to the vorticity extremum, and the spiral co-rotates with the vortex. As a consequence, for spiral arms with different launching points, the RWI explanation may be safely rejected.

However, it must be noted that the apparent launching point of the spiral, i.e. the origin of its detectable part, graphically indicated as a blue hatched mark, will depart from its physical origin, namely the vortex’s eye. For instance, Fig. 9 shows a $\sim 90^\circ$ discrepancy between the actual launching point and the the apparent origin of the main spiral arm. The figure also shows that, considering only spectral resolution as an experimental limitation, plane-RWI spirals are detectable as soon as the sensitivity is sufficient to resolve the vortex’s bulk signature. In short, spirals produce projected velocities just marginally smaller than the vortex’s bulk. We further note that plane-RWI spirals are a pure tracer of radial velocities v_r , which are observationally characterized by a change of sign in projected velocities across the major axis.

We note that the spiral’s pitch angle increases with h , as a consequence of a higher sound-speed. Hence, radial velocities are not self-similar across our models, as hotter disks produce higher Mach numbers, as illustrated in Fig. 12.

4. Discussion

4.1. Numerical VS practical differences

In Section 3.1, we showed that a promising data reduction strategy for vortex dynamic extraction in sharp density jumps was to subtract $\langle v_\phi \rangle$, and that the projected velocity seen on the major

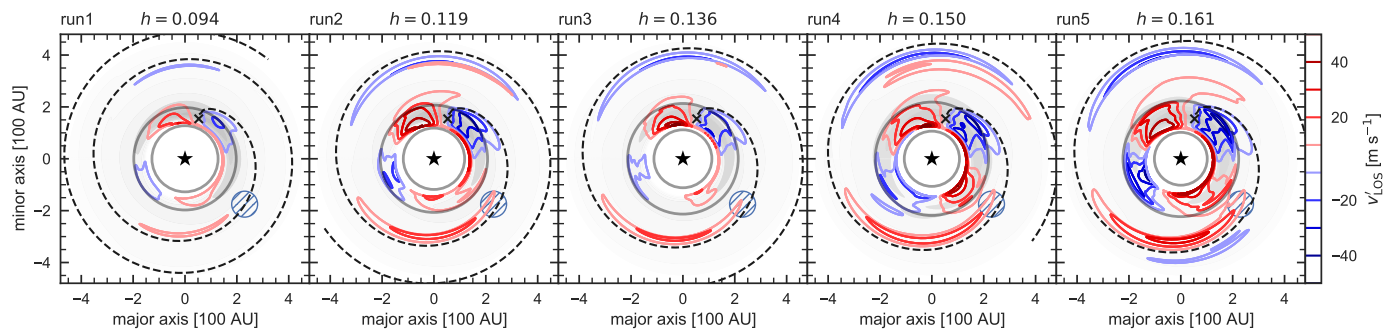


Fig. 9. A comparative view of v'_{LOS} with varying disk temperature h . Disk orientation is taken consistent with values found in the literature on HD 142527 ($i = 27^\circ$ Fukagawa et al. (2013), PA = 71° Kataoka et al. (2016)). Here we mock a spectral resolution of 12.5 m s^{-1} . The reference setup occupies the leftmost panel. Velocities in the cavity are masked as in Fig. 8. In dashed lines, we over-plot the best fit spirals following Huang et al. (2019) (eq. 2 therein), based on linear perturbation theory (Goldreich & Tremaine 1979; Rafikov 2002; Muto et al. 2012). Those fits were computed using $v_r = 0$ contours as input data. As a visual indicator, surface density is underplotted in greyscale. Additionally, grey circles indicate the $3\sigma_j$ region around the vortex eye, which is used later in Fig. 10. As in other figures, a black cross indicates the density maximum.

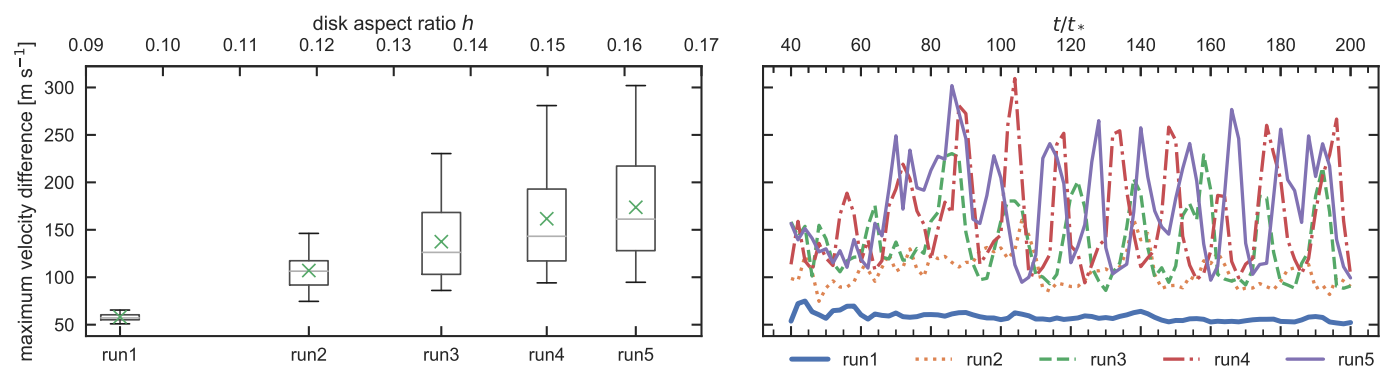


Fig. 10. Amplitude in v'_{LOS} across the annular region shown in Fig. 9, throughout the simulation time, represented as a boxplot (left). The whole time series is unraveled in the right panel. It is sampled every 2 orbital periods (the output rate of our simulations). Although the first run is remarkably constant, runs 3 to 5 exhibit significant dispersion within this metric, while the mean value (green crosses) itself is stabilized. These oscillations' period corresponds to the life-cycle of a secondary spiral arm, illustrated in Fig. 11.

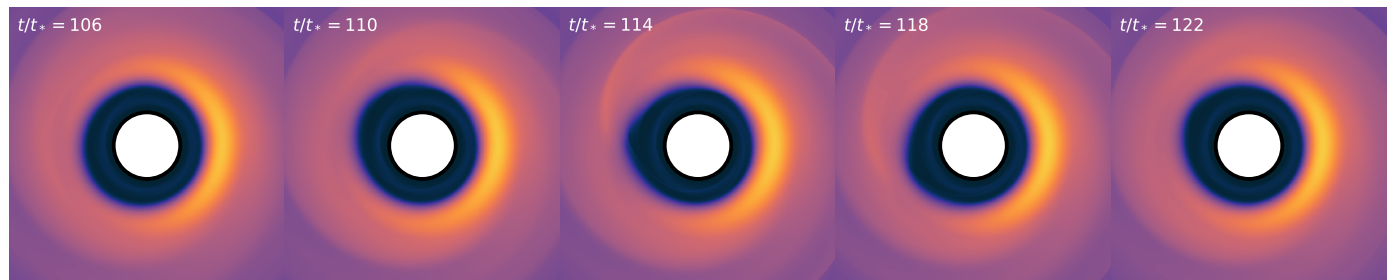


Fig. 11. Formation/dissipation cycle of a secondary spiral arm connected with disk eccentricity, illustrated for the most prominent case, run 5. Color maps density (same scale as Fig. 3). This secondary spiral is a transient and periodic phenomenon, responsible for large oscillations in maximum projected velocity as measured in Fig. 10

axis ($v_{\text{proj}}^{\text{maj}}$ for shorts) gives a reasonable proxy for it. In order to test the error implied by this approximation, this strategy is applied in Fig. 13. Consistently with our previous estimation, this more realistic view shows very little difference to the first, idealized one (Fig. 8). Figure 14 quantifies that 2D discrepancy as a difference between the numerical and practical cases. We find the discrepancy to reach at most $\sim 7 \text{ m s}^{-1}$.

4.2. Spiral detection

As shown in Section 3.4, the projected velocities seen in spiral arms are comparable in amplitude to those attained by the vortex's core. However, angular resolution might constitute an additional limitation to identify those secondary structures. In Fig. 15 we mock a limited angular resolution via Gaussian kernel convolution to the simulated velocity map, where the mean component of azimuthal velocity $\langle v_\varphi \rangle$ is subtracted prior to projection. We observe that the contrast sharpness of the main spiral pattern is altered but not destroyed by limited spatial resolution alone. We note that the spiral arm appears marginally broader in

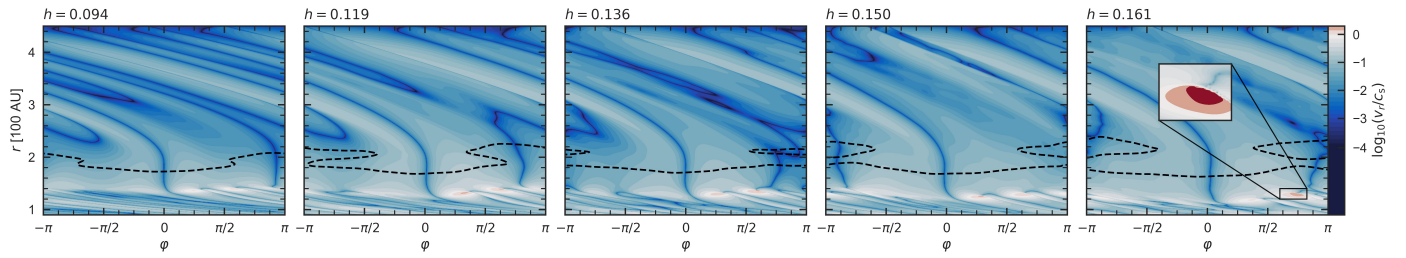


Fig. 12. Radial Mach number VS temperature (h), seen in polar coordinates. The colormapping is such that sub(super)-sonic regions appear in blue (red). The vortex center is always located at $\varphi = 0$. Dashed black lines indicate $v_\varphi = v_K$. The global structure is not self-similar when h varies, as one can see the keplerian line undergoes a reconnection as temperature increases, and spirals in the outer disk are shocking (Mach 1, white) closer to the vortex. Small super-sonic (red) regions are found in the inner region of the disk ($r \approx 120$ AU), as is highlighted in an inset in the rightmost panel. The flow remains sub-sonic everywhere else.

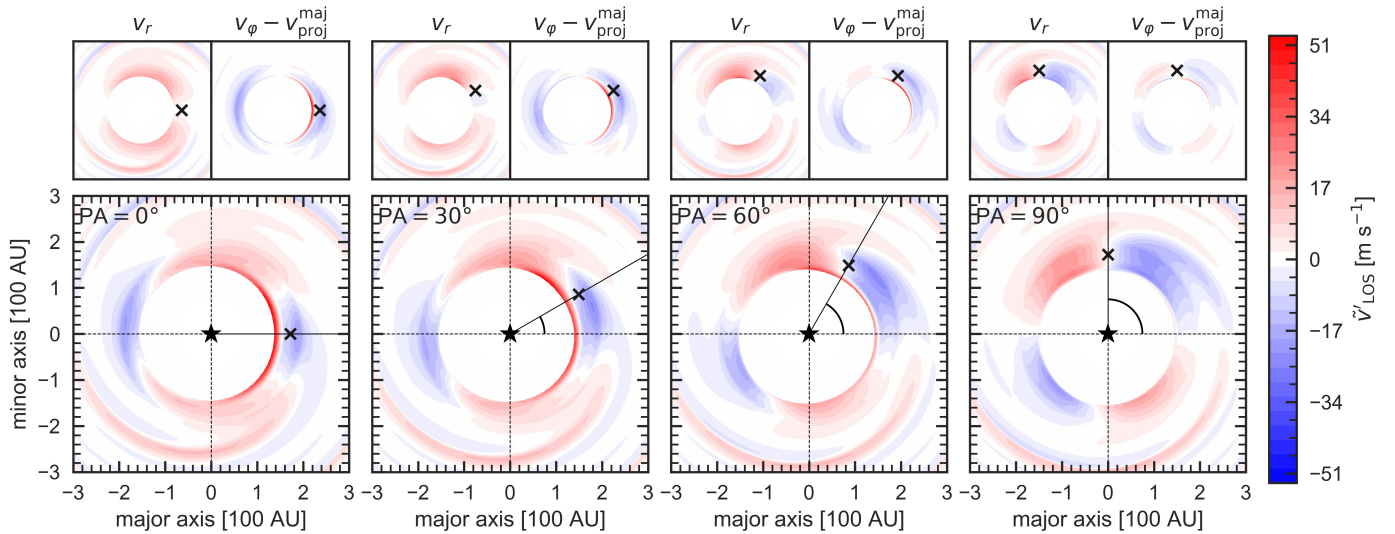


Fig. 13. A practical application of our data reduction method. The figure is similar to Fig. 8 except that $v_{\text{proj}}^{\text{maj}}$ is subtracted instead of $\langle v_\varphi \rangle$.

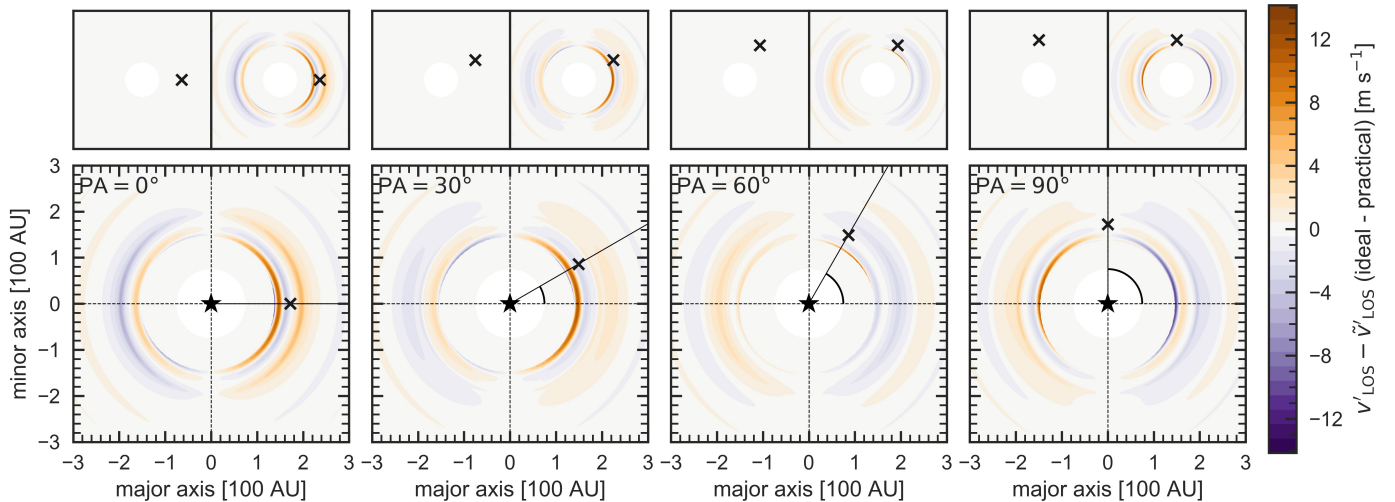


Fig. 14. Difference between numerical (Fig. 8) and practical (Fig. 13) cases. By construction, $v'_{\text{Los}} - \tilde{v}'_{\text{Los}}$ is a separable function $\text{err}(r, \varphi) = f(r) \cos(\varphi)$ where the density mask is axisymmetric.

Fig. 13 as compared with the numerical case Fig. 8. The velocity flip pattern however remains visible and is unaltered by the limited spatial resolution.

4.3. The origin of the cavity in HD 142527

The state of the art simulations for the thermal emission of HD 142527 were performed in Smooth-Particle Hydro (SPH) by Price et al. (2018), and do not feature vortex formation. This

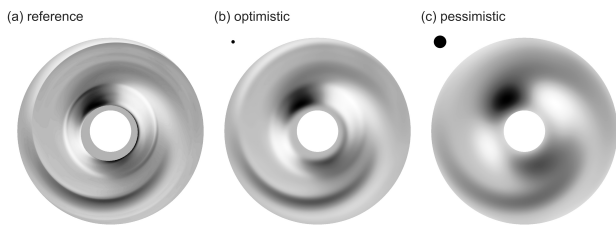


Fig. 15. A qualitative comparison between a simulation-precision velocity map (left), and against artificially lowered spatial resolution, simulation with a gaussian kernel convolution. We apply kernels with angular size (in proportions of the target's) 7% (center), and a 3 times larger one 21% (left). With HD 142527's distance, the center panel corresponds to the recent high resolution obtained by [Keppler et al. \(2019\)](#). No noise is added. Projected velocities are shown in linear grey-scale, where $v'_{\text{LOS}} < 0$ is light and $v'_{\text{LOS}} > 0$ is dark grey. Secondary spiral patterns are lost at low resolution but the primary remains visible. Beams size is shown as a black dot. The velocity map corresponds to the rightmost panel in [Fig. 9](#).

study was focused on explaining as many features as possible with the excitation provided by the eccentric stellar companion. However, it must be noted that SPH solvers generate numerical viscosities $\sim 10^{-2}$ [Arena & Gonzalez \(2013\)](#), much greater than typical values used in RWI vortex studies⁷ ([Lyra et al. 2009](#); [Hammer et al. 2017, 2019](#); [Ono et al. 2016](#)), so this possibility was inherently not included in their study. In the present work, we stayed agnostic regarding how the initial unstable density jump was formed. The stellar companion, while not included in our model, provides a plausible cause to the cavity. However, gravitational perturber-induced Rossby vortices have been studied in the context of circular orbital motion ([Li et al. 2005](#)). How eccentricity and inclination in the companion's orbit affects vortices formation, within an appropriately inviscid medium, remains to be studied.

4.4. Limits of this approach

An important limitation of the model is the lack of a vertical dimension. In a more realistic context, plane velocities (v_r, v_ϕ) are only detectable if the disk is inclined, which will in turn affect measurements by line-of-sight integration. This effect would however be mitigated by choosing optically thick molecular lines. Moreover, ([M eheut et al. 2012b](#)) showed that 3D vortices have a non negligible vertical velocity component while they form (typically 10% of the characteristic azimuthal velocity signature). As the RWI growth time is typically shorter than the vortex lifetime by one or two orders of magnitude, it seems reasonable to neglect vertical circulation.

It has been showed that the disk's contribution to the gravitational potential, promotes disk eccentricity ([Reg aly & Vorobyov 2017a](#)), which in turn amplifies the vortex's proper velocity. Because this effect is neglected in our model, we expect the resulting velocities to be slightly under-estimated here.

5. Conclusions

We showed that in cavity-hosting circumstellar disks, large eddies produce dynamical signatures on the verge of detectability for current facilities.

⁷ The model used in this paper is inviscid. We give insight on our evaluation of numerical viscosity in [Appendix B](#).

As a vortex' dynamical imprint resides in the non-axisymmetric part of the velocity field, it is crucial to the detection to be able to subtract the axisymmetric component from observations. In the case of a vortex formed at the inner edge of a cavity-hosting disk, a Keplerian power-law is not a correct proxy for the mean azimuthal velocity. This is because pressure gradients prone to vortex formation imply large deviations from keplerian velocities. Nevertheless, as projected velocities of the observational major axis directly map the azimuthal motion, a better mask can be obtained by averaging both sides of the velocity profile on this axis. This approach proved to produce small errors when compared with the actual azimuthal mean component of velocity $\langle v_\phi \rangle$. We also observed a saturation in the amplitude of projected velocities as temperature is increased. This result is to be taken with a grain of salt and may point to a limitation of the model we used. Using this amplitude as an estimator for spectral resolution requirement, we conclude that detection of a single large eddy is achievable under a 50 m s^{-1} to 150 m s^{-1} resolution, while the current maximal resolution with ALMA is $\sim 30 \text{ m s}^{-1}$. We stress that those minimal requirements were obtained within the particular case of the HD 142527 target, with a relatively low inclination (27°). Minimal resolution would be amplified by a factor 150% for a more likely, mean inclination of 45° , ceteris paribus. This demanding requirement may explain the current difficulty to elucidate the nature of known dust clumps in cavity-hosting disks, yet is achievable with existing facilities. Vortex-free mechanisms could also explain their formation, although observational constraints for fine gas dynamics are needed in order to properly discriminate concurrent scenarios.

Full 3D modeling would naturally extend the present work, and allow the study of second order effects in line-of-sight integration.

Acknowledgements. C.M.T. Robert's Ph.D. grant is part of ANR number ANR-16-CE31-0013 (Planet-Forming-Disks). Computations were performed with OCCIGEN CINES (allocation DARI A0060402231), and "M esocentre SIGAMM", hosted by Observatoire de la C ote d'Azur. The data presented in this work were proceeded and plotted with Python's data science ecosystem `scipy`, `numpy` ([van der Walt et al. 2011](#)), `matplotlib` ([Hunter 2007](#)), `pandas` ([McKinney 2010](#)) as well as `astropy` ([Robitaille et al. 2013](#); [Price-Whelan et al. 2018](#)), and the `yt` framework ([Turk et al. 2011](#)). C.M.T. is thankful to Aur elien Crida and Elena Lega for their early proofreading. The authors wish to thank the referee, Zsolt Reg aly, for helping improving the quality of the paper.

References

- Adams, F. C. & Watkins, R. 1995, *ApJ*, 451, 314
- Andrews, S. M., Terrell, M., Tripathi, A., et al. 2018, *ApJ*, 865, 157
- Arena, S. E. & Gonzalez, J.-F. 2013, *Mon Not R Astron Soc*, 433, 98
- Ataiee, S., Dullemond, C. P., Kley, W., Reg aly, Z., & Meheut, H. 2014, *A&A*, 572, A61
- Ataiee, S., Pinilla, P., Zsom, A., et al. 2013, *A&A*, 553, L3
- Avenhaus, H., Quanz, S. P., Schmid, H. M., et al. 2014, *ApJ*, 781, 87
- Barge, P. & Sommeria, J. 1995, *A&A*, 295, L1
- Baruteau, C., Barraza, M., P erez, S., et al. 2019, *MNRAS*, 486, 304
- Benisty, M., Juhasz, A., Facchini, S., et al. 2018, *A&A*, 619, 171
- Biller, B., Lacour, S., Juhasz, A., et al. 2012, *ApJ Lett.*, 753, L38
- Birnstiel, T., Dullemond, C. P., & Pinilla, P. 2013, *A&A*, 550, L8
- Boehler, Y., Weaver, E., Isella, A., et al. 2017, *ApJ*, 840, 60
- Bracco, A., Chavakis, P. H., Provenzale, A., & Spiegel, E. A. 1999, *Physics of Fluids*, 11, 2280
- Casassus, S., Marino, S., Lyra, W., et al. 2019, *MNRAS*, 483, 3278
- Casassus, S., Marino, S., P erez, S., et al. 2015a, *ApJ*, 811, 92
- Casassus, S. & P erez, S. 2019, *The Astrophysical Journal Letters*, 883, L41
- Casassus, S., P erez M., S., Jord an, A., et al. 2012, *ApJ Lett.*, 754, L31
- Casassus, S., Wright, C., Marino, S., et al. 2015b, *ApJ*, 812, 126
- Cazzoletti, P., van Dishoeck, E. F., Pinilla, P., et al. 2018, *A&A*, 619, A161
- Chiang, E. & Youdin, A. 2010, *Annu. Rev. Earth Planet. Sci.*, 38, 493

- Christiaens, V., Casassus, S., Perez, S., van der Plas, G., & Ménard, F. 2014, *ApJL*, 785, L12
- de Val-Borro, M., Artymowicz, P., D'Angelo, G., & Peplinski, A. 2007, *A&A*, 471, 1043
- de Val-Borro, M., Edgar, R. G., Artymowicz, P., et al. 2006, *MNRAS*, 370, 529
- Dong, R., Liu, S.-Y., Eisner, J., et al. 2018, *ApJ*, 860, 124
- Fu, W., Li, H., Lubow, S., & Li, S. 2014, *ApJ Lett.*, 788, L41
- Fukagawa, M., Tamura, M., Itoh, Y., et al. 2006, *ApJ*, 636, L153
- Fukagawa, M., Tsukagoshi, T., Momose, M., et al. 2013, *Publ Astron Soc Jpn Nihon Tenmon Gakkai*, 65
- Gaia Collaboration, Brown, A. G. A., Vallenari, A., et al. 2016, *A&A*, 595
- Goldreich, P. & Tremaine, S. 1979, *The Astrophysical Journal*, 233, 857
- Hammer, M., Kratter, K. M., & Lin, M.-K. 2017, *MNRAS*, 466, 3533
- Hammer, M., Pinilla, P., Kratter, K. M., & Lin, M.-K. 2019, *MNRAS*, 482, 3609
- Harten, A., Lax, P. D., & van Leer, B. 1983, *SIAM Rev.*, 25, 35
- Huang, P., Dong, R., Li, H., Li, S., & Ji, J. 2019, *ApJ*, 883, L39
- Hunter, J. D. 2007, *Comput. Sci. Eng.*, 9, 99
- Isella, A., Huang, J., Andrews, S. M., et al. 2018, *ApJL*, 869, L49
- Kataoka, A., Tsukagoshi, T., Momose, M., et al. 2016, *ApJ Lett.*, 831
- Keppler, M., Teague, R., Bae, J., et al. 2019, *A&A*, 625, A118
- Koren, B. 1993, *Rep.-Dep. Numer. Math.*, 1
- Lai, D. & Tsang, D. 2009, *MNRAS*, 393, 979
- Li, H., Colgate, S. A., Wendroff, B., & Liska, R. 2001, *ApJ*, 551, 874
- Li, H., Finn, J. M., Lovelace, R. V. E., & Colgate, S. A. 2000, *ApJ*, 533, 1023
- Li, H., Li, S., Koller, J., et al. 2005, *ApJ*, 624, 1003
- Lin, M. 2012, *AGU Fall Meeting Abstracts*, 21, P21B
- Lovelace, R. V. E., Li, H., Colgate, S. A., & Nelson, A. F. 1999, *ApJ*, 513, 805
- Lyra, W., Johansen, A., Klahr, H., & Piskunov. 2009, *A&A*, 493, 1125
- McKinney, W. 2010, in *Proceedings of the 9th Python in Science Conference*, 51–56
- McNally, C. P., Nelson, R. P., & Paardekooper, S.-J. 2018, *MNRAS*, 477, 4596
- Méheut, H., Keppens, R., Casse, F., & Benz, W. 2012a, *A&A*, 542, A9
- Méheut, H., Yu, C., & Lai, D. 2012b, *MNRAS*, 422, 2399
- Montesinos, M., Perez, S., Casassus, S., et al. 2016, *Astrophys. J. Lett.*, 823, L8
- Muto, T., Grady, C. A., Hashimoto, J., et al. 2012, *ApJL*, 748, L22
- Ono, T., Muto, T., Takeuchi, T., & Nomura, H. 2016, *ApJ*, 823, 84
- Pérez, S., Casassus, S., Hales, A., et al. 2020, *ApJL*, 889, L24
- Perez, S., Casassus, S., Ménard, F., et al. 2015, *ApJ*, 798, 85
- Pineda, J. E., Szulágyi, J., Quanz, S. P., et al. 2019, *ApJ*, 871, 48
- Pinte, C., Price, D. J., Ménard, F., et al. 2018, *ApJ Lett.*, 860, L13
- Pinte, C., van der Plas, G., Ménard, F., et al. 2019, *Nat Astron*, 1
- Porth, O., Xia, C., Hendrix, T., Moschou, S. P., & Keppens, R. 2014, *ApJ Suppl Ser*, 214, 4
- Price, D. J., Cuello, N., Pinte, C., et al. 2018, *MNRAS*, 477, 1270
- Price-Whelan, a. A. M., Sip\Hocz, B. M., Günther, H. M., et al. 2018, *AJ*, 156, 123
- Rafikov, R. R. 2002, *ApJ*, 572, 566
- Rameau, J., Chauvin, G., Lagrange, A.-M., et al. 2012, *A&A*, 546, A24
- Rayleigh, J. W. 1879, *Proc. Lond. Math. Soc.*, 1, 57
- Regály, Z., Juhasz, A., Sándor, Z., & Dullemond, C. P. 2012, *MNRAS*, 419, 1701
- Regály, Z., Sándor, Z., Csomós, P., & Ataiee, S. 2013, *MNRAS*, 433, 2626
- Regály, Z. & Vorobyov, E. 2017a, *A&A*, 601, A24
- Regály, Z. & Vorobyov, E. 2017b, *MNRAS*, 471, 2204
- Richard, S., Barge, P., & Le Dizès, S. 2013, *A&A*, 559, A30
- Robitaille, T. P., Tollerud, E. J., Greenfield, P., et al. 2013, *A&A*, 558, A33
- Shakura, N. I. & Sunyaev, R. A. 1973, *A&A*, 500, 33
- Tanga, P., Babiano, A., & Dubrulle, B. 1996, *Icarus*, 121, 158
- Teague, R., Bae, J., Bergin, E. A., Birnstiel, T., & Foreman-Mackey, D. 2018a, *ApJL*, 860, L12
- Teague, R., Bae, J., Birnstiel, T., & Bergin, E. A. 2018b, *ApJ*, 868, 113
- Teague, R. & Foreman-Mackey, D. 2018, *Res. Notes Am. Astron. Soc.*, 2, 173
- Teague, R., Guilloteau, S., Semenov, D., et al. 2016, *A&A*, 592, A49
- Turk, M. J., Smith, B. D., Oishi, J. S., et al. 2011, *ApJ Suppl. Ser*, 192, 9
- van der Marel, N., van Dishoeck, E. F., Bruderer, S., et al. 2016, *A&A*, 585, A58
- van der Walt, S., Colbert, S. C., & Varoquaux, G. 2011, *Comput. Sci. Eng.*, 13, 22
- Verhoeff, A. P., Min, M., Pantin, E., et al. 2011, *A&A*, 528, A91
- Xia, C., Teunissen, J., Mellah, I. E., Chané, E., & Keppens, R. 2018, *ApJ Suppl Ser*, 234, 30
- Yen, H.-W., Liu, H. B., Gu, P.-G., et al. 2016, *ApJ Lett.*, 820, L25
- Zhu, Z. & Baruteau, C. 2016, *MNRAS*, 458, 3918
- Zhu, Z. & Stone, J. M. 2014, *ApJ*, 795, 53

Appendix A: Aspect ratios evaluations

Appendix A.1: Equivalence to locally isothermal

Our model differs from the widely used locally isothermal prescription in that it is not defined in terms of scale-height

$$H = hr(r/r_*)^\beta, \quad (\text{A.1})$$

where h is the disk aspect ratio and β is the flaring. We can nonetheless draw an equivalence with those parameters for the power law density distribution at the core of Eq. (3), such that $\Sigma(r) = \Sigma_0(r/r_*)^{-1}$. In the locally isothermal prescription, the scale height is usually defined such that $H^2 = c_s^2/\Omega_K^2$, so we can equate this with Eq. (A.1) to get

$$\begin{aligned} h^2 r^2 (r/r_*)^{2\beta} &= \frac{\gamma p / \Sigma}{GM/r^3} \\ &= \frac{\gamma S}{GM} r^3 \Sigma^{\gamma-1} \\ &= \frac{\gamma S \Sigma_0^{\gamma-1}}{GM} r^3 (r/r_*)^{1-\gamma}. \end{aligned} \quad (\text{A.2})$$

at which point we deduce an effective aspect ratio and disk flaring, in terms of the actual simulation parameters

$$\begin{cases} h^2 &= \frac{\gamma S \Sigma_0^{\gamma-1} r_*}{GM}, \\ \beta &= 1 - \gamma/2 = 1/6. \end{cases} \quad (\text{A.3})$$

We note that our fixed resolution corresponds to $\Delta r/H(r_j) \approx 0.04$ for the reference model. Figure A.1 shows the resulting variation in h as we scale up Σ_0 , following Eq. (A.3).

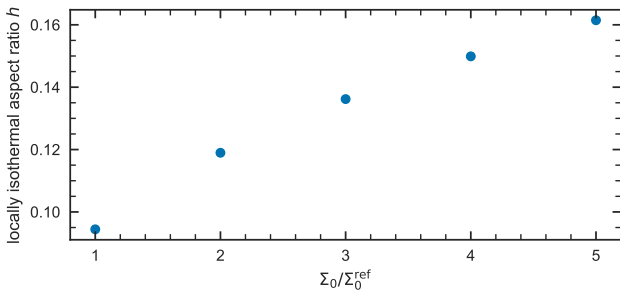


Fig. A.1. Correspondence between locally isothermal aspect ratio and "disk mass" in our simulations. The leftmost model is the reference.

Appendix A.2: Spiral fitting

In Fig. 9, we fitted the linear-regime spiral wave shape (Goldreich & Tremaine 1979; Rafikov 2002; Muto et al. 2012) given by

$$\begin{aligned} \varphi(r) &= \varphi_o - \frac{\text{sgn}(r - r_o)}{H_o} \times \\ &\left((r/r_o)^{1+\beta} \left[\frac{1}{1+\beta} - \frac{1}{1-\alpha+\beta} (r/r_o)^{-\alpha} \right] - \left[\frac{1}{1+\beta} - \frac{1}{1-\alpha+\beta} \right] \right), \end{aligned} \quad (\text{A.4})$$

where α, β are power-law exponents respectively defined as $\Omega \propto r^{-\alpha}$ and $c_s \propto r^{-\beta}$. (r_o, φ_o) are the spiral origin's coordinates, while H_o is a scale-height at this position. The fit was performed with H_o as a free parameter, so we the corresponding aspect ratio, differs from the locally isothermal equivalent h value used throughout the paper and described in the previous section. Figure A.2 shows values against each other.

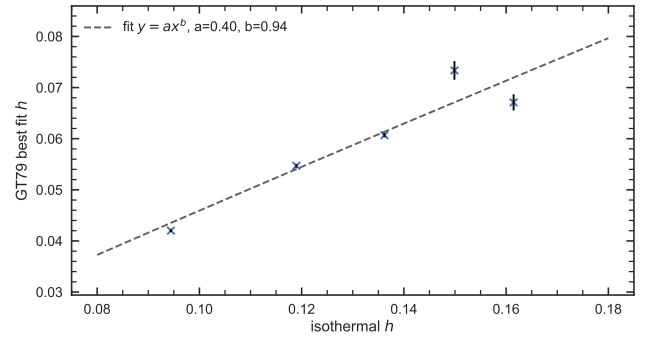


Fig. A.2. Aspect ratios as defined in Appendix A.1 VS empirical values obtained from fitting Equation (A.4). The later is roughly 40% of the former.

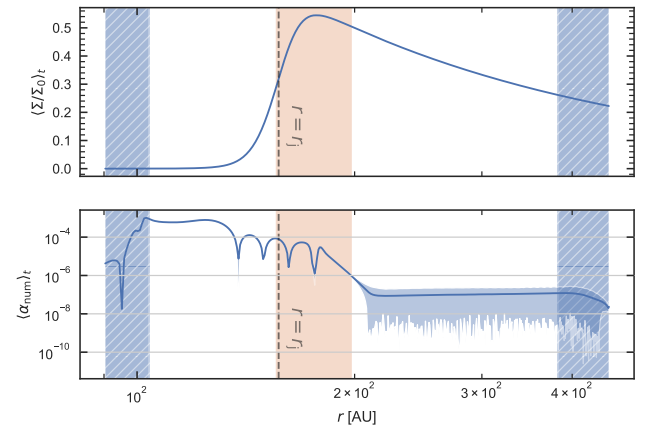


Fig. B.1. Density (top) and numerical viscosity equivalent α value (bottom) time-averaged over 10 orbital periods ($t/t_* \in [90, 100]$) with a sampling rate of 0.1 orbital periods. The solid blue shadows indicate the variation interval over the sample timeseries, showing that the profile is very stable in the region of interest. Hatched regions highlight the wave killing zones, while the orange region loosely indicates the vortex forming region, spanning one scale height away from the local density maximum.

Appendix B: Numerical viscosity evaluation

In order to estimate numerical viscosity $\nu_{\text{num}}(r)$, performed a 1D in a 1D run, with identical parameterization as our reference 2D run (run1). The analytical initial conditions constitute a stable equilibrium since RWI can not grow in 1D. Since our boundary conditions do not impose mass flux, any radial mass transport \dot{M} through the simulation domain is caused by numerical viscosity such that $\nu_{\text{num}}\Sigma = |\dot{M}|/3\pi$. In terms of Shakura & Sunyaev (1973)'s alpha viscosity model $\nu_{\text{num}} = \alpha_{\text{num}} H c_s$, so finally

$$\alpha_{\text{num}} = \frac{2}{3} \left| \frac{v_r}{h c_s} \right|. \quad (\text{B.1})$$

The obtained profile, time-averaged, is plotted in Fig. B.1. Highest numerical viscosities ($\sim 2 \times 10^{-3}$) are reached in the cavity, while it stays bounded $< 10^{-4}$ in the vortex-forming region, roughly represented in orange.